buildings

MDPI

Article

Model Testing for Bending Performance on Fragile Cross-Section of Square Hollow Steel-Reinforced Concrete Column

Hulin Li [1], Yang Zhou [2,*], Shenglin Geng [2], Haijiang Qin [1], Xiong Wang [1] and Jinpeng Li [1]

[1] Shanghai Baoye Group Co., Ltd., Shanghai 200941, China; linghu1111@163.com (H.L.)
[2] College of Civil Engineering, Henan University of Technology, Zhengzhou 450001, China
* Correspondence: robertzhouy@haut.edu.cn

Abstract: This study researches the bending and shear performance of the fragile cross-section of square hollow steel-reinforced concrete columns using experiments, numerical analysis, and theoretical investigation. First, three tests of square hollow steel-reinforced concrete column (HSrCC) specimens considering different sectional sizes and grouting conditions were conducted. The bearing capacity and load transfer mechanisms under bending and shear loading were experimentally compared. Second, a numerical model was established based on the experimental results, and then parametric studies were performed on the bearing capacity and deformation of the structure. Last, a peak load calculation formula was derived in this study considering thickness and strength for a 400 × 400 square HSrCC. Based on the experimental results, the failure process of the specimen can be divided into four steps. Grouting increases stiffness at the front part of the specimen but induces significant damage at the rear compared to the no-grouting case, with the maximum strain increasing by 25%. Increasing the cross-sectional area of the concrete short column effectively improves the overall performance, with the maximum tensile strain of the concrete short column being reduced by approximately 1.2 times. Under the given sectional dimensions, parametric analysis suggests that the optimal square hollow steel thickness and steel strength range from 14 mm to 16 mm and from Q355 to Q420, respectively. The proposed peak load calculation formula demonstrates a discrepancy of less than 5.06% when compared with the numerical model results. These findings provide valuable references for the design of square hollow steel-reinforced concrete columns.

Keywords: square hollow steel-reinforced concrete columns; bending performance; prefabricated structure; numerical analysis; parametric analysis

check for updates

Academic Editor: Grzegorz Ludwik Golewski

Received: 23 December 2024
Revised: 13 January 2025
Accepted: 19 January 2025
Published: 21 January 2025

Citation: Li, H.; Zhou, Y.; Geng, S.; Qin, H.; Wang, X.; Li, J. Model Testing for Bending Performance on Fragile Cross-Section of Square Hollow Steel-Reinforced Concrete Column. *Buildings* **2025**, *15*, 313. https://doi.org/10.3390/buildings15030313

Copyright: © 2025 by the authors. Licensee MDPI, Basel, Switzerland. This article is an open access article distributed under the terms and conditions of the Creative Commons Attribution (CC BY) license (https://creativecommons.org/licenses/by/4.0/).

1. Introduction

In recent years, prefabricated buildings have developed rapidly. In addition, among them, steel structure is one of the widely selected prefabricated buildings due to its light weight, high strength, and environmental friendliness. The steel structures are assembled through welding or bolting, which enables fast construction of superstructures. The steel structures can be combined with concrete as a composite structure to meet the design requirements of large-span or super high-rise buildings. The use of steel-concrete composite structures effectively combines the strengths of both materials, meanwhile provides benefits of convenient connections, high load-bearing capacity, excellent deformation performance, superior seismic resistance, and reliable fire and heat resistance [1,2]. Consequently, this structural system has attracted significant attention from researchers and engineers in recent years. Concrete-filled tube (CFT) is one of the most widely employed steel-concrete

composite structures. Existing research on CFT structures, primarily focusing on the axial compression performance [3–7], l seismic performance [8–10], and connection methods and performance of joints [11–14], has revealed that CFT columns exhibit enhanced load-bearing and deformation resistance capabilities and excellent ductility. The integration of steel tube and filled concrete effectively reduces the torsional effects, promoting the related design for prefabricated structures.

Among all kinds of CFTs, the concrete-filled square tube (also called a square steel-reinforced concrete column and CFST), as its larger moment of inertia compared to a circular tube, presents superior bending resistance [15] during extensive applications. CFST combines the benefits of traditional steel and concrete columns and has been implemented in numerous super high-rise structures [16–19]. It is primarily used for columns, beams, and beam-column connections in these structures because of its high strength and regular cross-section. Zhang et al. [20] analyzed the influence of torsion on CFST and derived a formula to calculate the torsional rigidity. Jia et al. [21] aimed to assess the structural behavior of CFST columns under long-term sustained loads and propose corresponding design methods. Zhou et al. [22] used ABAQUS simulations to explore the differences in cyclic shear behavior between stiffened and unstiffened square thin-walled CFST columns and investigated the failure mechanisms of CFST. Hu et al. [23] investigated the confinement effect and stress-strain model for concrete in multi-cell CFST columns under axial compression. The above study all mentions that CFST has a good ability to resist deformation and is widely applicable in the field of steel structures. In addition, some researchers have designed and proposed the use of bond slip [24] and CFRP [25] to reinforce structures. These measures can improve the mechanical properties of concrete, thereby contributing to the enhancement of the structural load-bearing capacity.

In combination with a local practical project, one issue of CE-CFT is the tedious procedure of filling the concrete into the tube one by one and finally delaying the construction time of the whole project. The building time will be significantly shortened if the CE-CFT under ±0.00 elevation could be replaced by the hollow steel-reinforced concrete column (HSrCC) without concrete filling (Figure 1). However, this setup of HSrCC in Figure 1 was rarely reported. It wonders whether the square HSrCC could function well and what its features are under bending and shear loading.

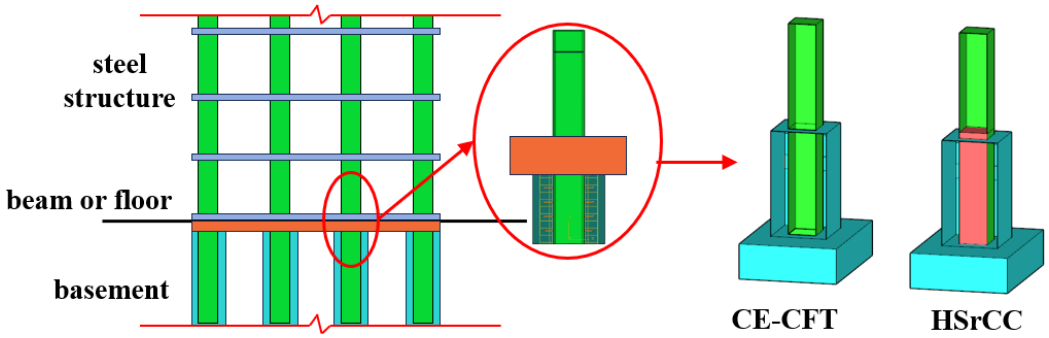

Figure 1. The details of the prefabricated steel structure.

As mentioned above, the HSrCC in Figure 1 is unique in the project, and research about its shear and bending resistance was desired all the time. This study aims to explore the mechanical behavior of HSrCC subjected to lateral loading. First, three tests of square steel-reinforced concrete column specimens considering different sectional sizes and concrete-filling conditions were conducted. The bearing capacity and load transfer mechanisms under bending and shear loading were experimentally compared under different encasement thicknesses and grouting conditions. Second, a numerical model was established based on the experimental results, and then a parametrical study was performed to

analyze the bearing capacity and deformation of the HSrCC with varied factors. Last, a peak load calculation formula was derived in this study considering thickness and strength for a 400 × 400 square HSrCC.

2. Experimental Design

2.1. Specimen Details

There are 3 specimens used in this section, namely SC1, SC2, and SC3. The specimen primarily consists of 3 components: a steel tube, concrete short columns, and a supporting concrete bases. The steel tube is a square hollow steel column with a cross-sectional size of 400 mm × 400 mm × 14 mm and a height of 3000 mm, which refers to a real local project. The tube can be separated into 2 sections, a 1500 mm-high upper part and a 1500 mm-high lower part. The lower part was encased with concrete. The base has a size of 2000 mm × 1400 mm × 500 mm. In SC1 (Figure 2), the encased concrete at the lower part has an outer size of 800 mm × 800 mm. In SC2, all the settings and dimensions are the same as SC1, but with concrete filling into the tube up to a height of 1550 mm from the bottom, i.e., 50 mm above the encased-concrete top. In SC3, the tube is hollow, but the encased concrete was enlarged with a size of 900 mm × 900 mm, i.e., with a larger thickness of encasement. The detailed information of the specimens is provided in Table 1.

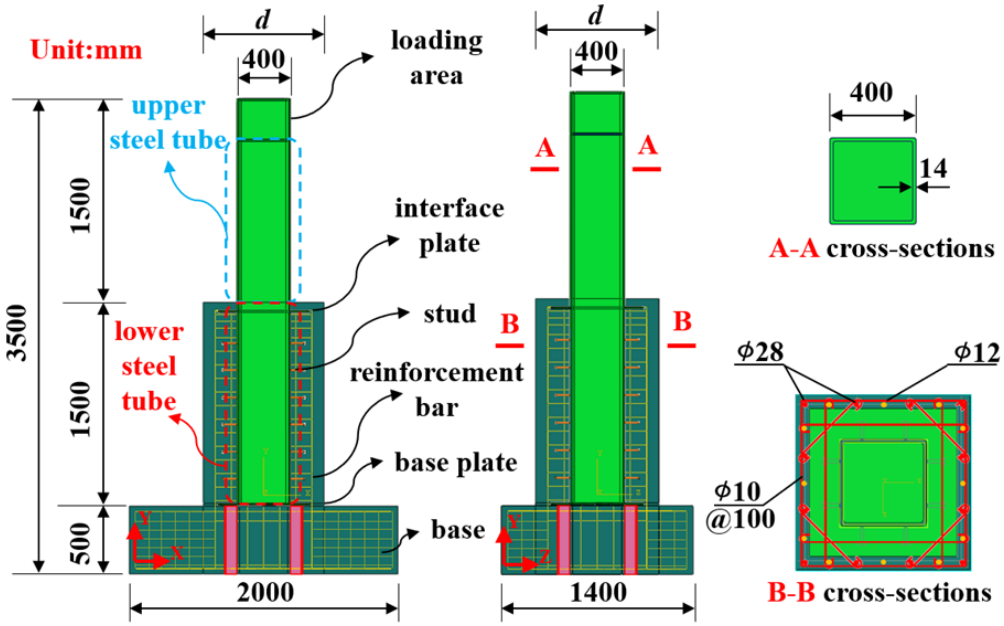

Figure 2. The details of the specimen's dimension.

Table 1. The main dimension of the specimens.

Number	Tube Thickness/mm	Tube Size/mm^2	Outer Size of Concrete Column/mm^2	Hollow
SC1	14	400 × 400	800 × 800	Yes
SC2			800 × 800	No
SC3			900 × 900	Yes

The longitudinal reinforcement of the concrete short column was arranged around the steel tube, consisting of 12 pieces of 28 mm diameter steel bars. Between every two 28 mm bars, one 12 mm bar was placed, totaling 12 such bars. The stirrups for the short concrete column are 10 mm diameter steel bars, spaced at 100 mm intervals along the Y-direction. Tie bars were arranged at regular intervals.

First, before casting, the prefabricated steel tube was delivered to the campus and connected with the basement reinforcement (Figure 3a). The strain gauges were applied to the steel tube and reinforcement bars and then were fixed using gauze and epoxy resin. The bar surface was prepared by grinding previously. Second, the base casting was performed and cured for 7 days (Figure 3b). Third, the formwork and casting of the short column concrete were conducted (Figure 3c). The concrete shrinkage was not considered. Then, surface strain gauges were applied on the concrete surface. Last, wiring, specimen fixation, and installation of the loading device were performed in the laboratory (Figure 3d).



Figure 3. The detailed process of specimen fabrication, (**a**) formwork and reinforcement installation; (**b**) base casting; (**c**) column casting; (**d**) wiring, specimen fixation, and installation.

Of note, stiffening plates are installed at the bottom and at the interface with the concrete short column to further increase the structural resistance, named the interface plate and base plate. The studs are arranged in the encased concrete between the two stiffening plates. The bottom stiffening plate and the reinforcement bars were fixed before concrete pouring to make the base and column an integrity. During the specimen casting, standard concrete cube test blocks were reserved for strength testing. After 28-days of curing the test cube of 150 mm × 150 mm × 150 mm, the axial compressive strength of the concrete of f_{cu} = 37.4 MPa was measured on average. In addition, the yield strength of the steel was 355 MPa obtained from the provider.

2.2. Loading Method

The experiment was conducted using the "L-shaped" reaction wall and a 250-ton actuator (MTS) in the Structural Laboratory of Henan University of Technology [26]. The lateral load was applied to the top end of the specimen using the MTS actuator (Figure 4) with a loading rate of 0.01 mm/s, maintained for 5 min for every step. In addition, each step was corresponding to 0.2 mm. In the actual working conditions, the concrete short column is constrained by a rigid ground beam subjected to unidirectional force. Under this circumstance, four bolt rods extended from the reaction wall, and a steel beam was placed in front of the concrete short column to impose a certain amount of displacement and rotation constraints. Three identical steel beams were placed beneath the specimen during the experiment to level up the specimen to the desired height. In addition, ground anchor rods were used to fully secure the setup to the floor, as shown in Figure 4.

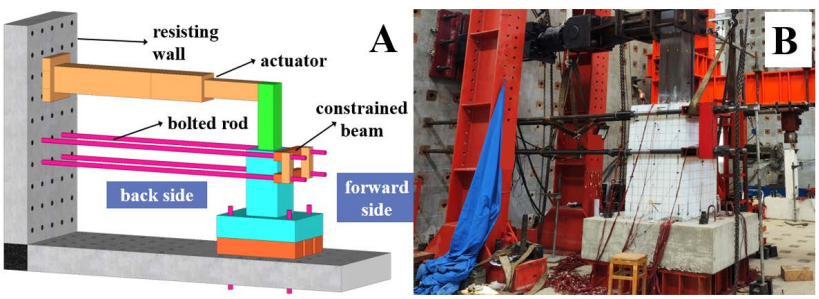

Figure 4. Loading mode, (**A**) schematic view; (**B**) photo.

2.3. Monitoring

To capture the stress characteristics of various parts of the square HSrCC under shear forces, as well as the strain features at the contact surface (i.e., the fragile section) between the concrete column and the square hollow steel, strain gauges were arranged on the surfaces of different components as shown in Figure 5a,b. These gauges recorded the development of stress during loading. Strain gauges were also placed along the longitudinal reinforcement inside the concrete column to assess the impact of shear force on reinforcement bars. The arrangement of the measurement points is shown in Figure 5c. On the top of the interface plate (including around the concrete zone) and the base plate, strain gauges were also set up to investigate the response of the stiffening plate. In addition to the strain gauges, displacement transducers were placed on the front side of the square hollow steel and the constraint beam to measure the later deformation at these two positions. During testing, the surface crack propagation was monitored and recorded.

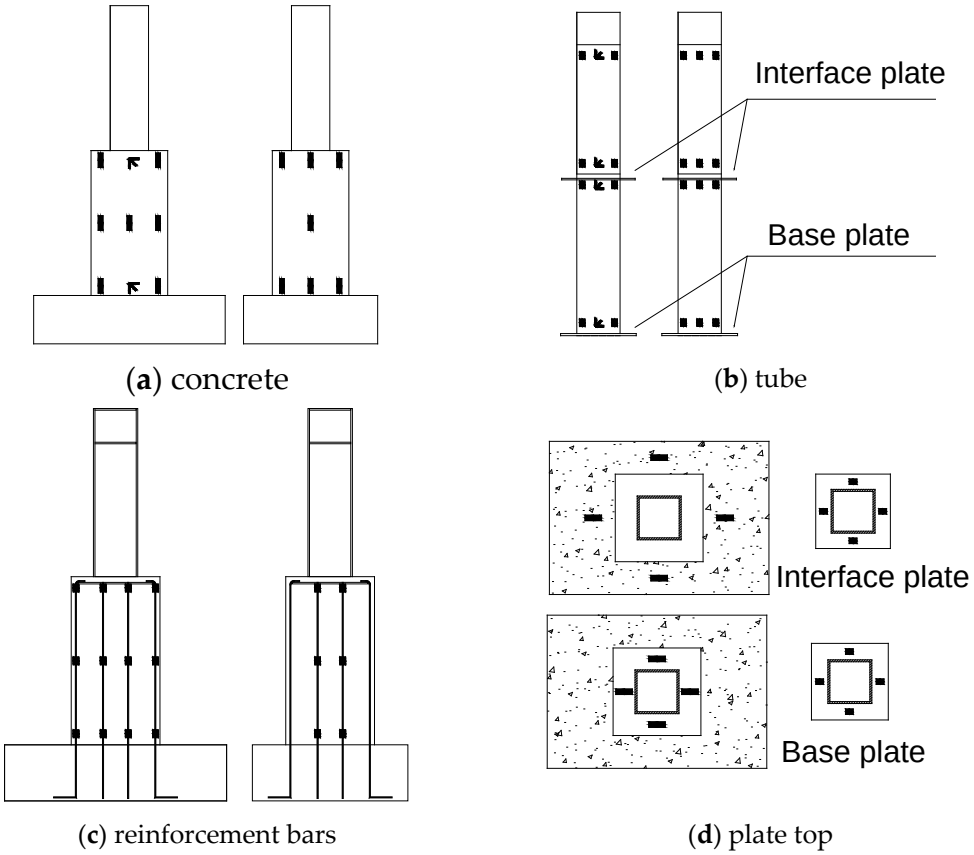

(**a**) concrete (**b**) tube

(**c**) reinforcement bars (**d**) plate top

Figure 5. Strain gauge measuring point arrangement.

3. Experimental Results and Analysis

3.1. Failure Behavior

3.1.1. Crack Propagation of Concrete

The overall crack propagation was analyzed to first study the failure mechanism of the specimens. The final crack propagation can be seen in Figure 6. In general, the three specimens exhibited similar crack propagation processes: (1) initial crack between encased concrete and tube; (2) transverse crack at top of concrete column; (3) transverse crack on the side surface of concrete column; (4) crack of concrete base; (5) crushing at constrained beam. (1) Initial crack between encased concrete and tube. The initial crack was observed at the contact point between the concrete short column and tube corner at mid-height, i.e., 1.5 m high, where stress concentration caused slight bulging of the concrete and formation of

cracks. (2) Transverse crack at top of concrete column. With continuous loading, the crack at the tube corner became dense, and finally transverse cracks formed on the top surface of the concrete short column. (3) Transverse crack on the side surface of concrete column. As the loading continued, with lateral deformation of the tube, transverse cracks developed on the tension side (backside in Figure 3) of the concrete column. (4) Crack of concrete base. When the displacement applied reached approximately 35 mm, the significant crack was observed on the concrete base. (5) Crushing at constrained beam. With increasing loading, the contact surface between the concrete short column and the constraint beams experienced gradual crushing. Meanwhile, in this step, the damage of the specimen further progressed, leading to the buckling of the upper steel tube.

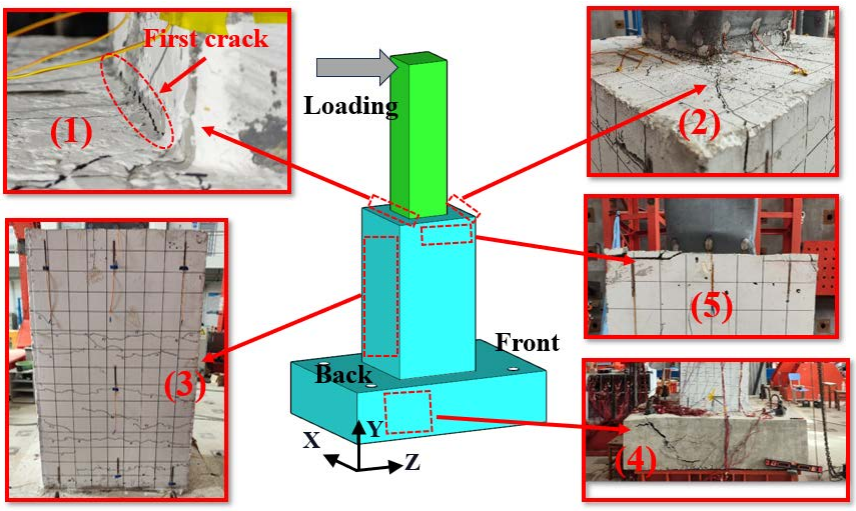

Figure 6. Typical crack propagation of concrete columns of the specimens.

Comparing the measurement points with the highest strain on the forward side and back sides of the concrete short columns for each specimen, as shown in Figure 7, it is observed that the maximum compressive and tensile strain of SC3 is close to each other, indicating a more uniform strain distribution compared to SC1 and SC2. This suggests that increasing the cross-section of the concrete short column can effectively reduce structural deformation. The backside of SC2 exhibits the highest tensile strain, reaching 0.018% at 600 kN, which is approximately 20% higher than that of SC1 and 55% higher than that of SC3, indicating that filling concrete may lead to increased deformation of the concrete short column.

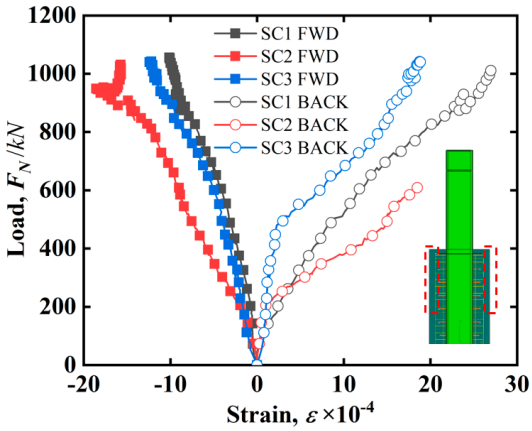

Figure 7. Strain comparisonat back side (BACK) and forward side (FWD) of concrete short column.

3.1.2. Deformation of Tube

The deformation features of the tube at the interface for all three specimens were shown as in Figure 8a. All three specimens exhibited significant normal buckling deformation on the front side at the bottom of the upper steel tube, with SC1 and SC2 showing outward bulging and SC3 showing inward concaving, and the overall strain was almost the same (Figure 8b). However, from the strain of the lower steel tube (Figure 8c), SC1 and SC3 had the same strain level, while SC2 showed a large tensile strain on the back side, indicating uneven stress distribution between the front and back. The three specimens also exhibited normal buckling on the sides of the lower portion of the upper steel tube. Due to filled concrete, the deformation of the SC2 specimen was not significant, while the SC1 specimen exhibited inward concaving and the SC3 specimen showed outward bulging. From these observations, it can be concluded that filling concrete or not has little effect on the buckling of the steel tube. Filling concrete or not will not significantly impact the strength and failure of the specimen.

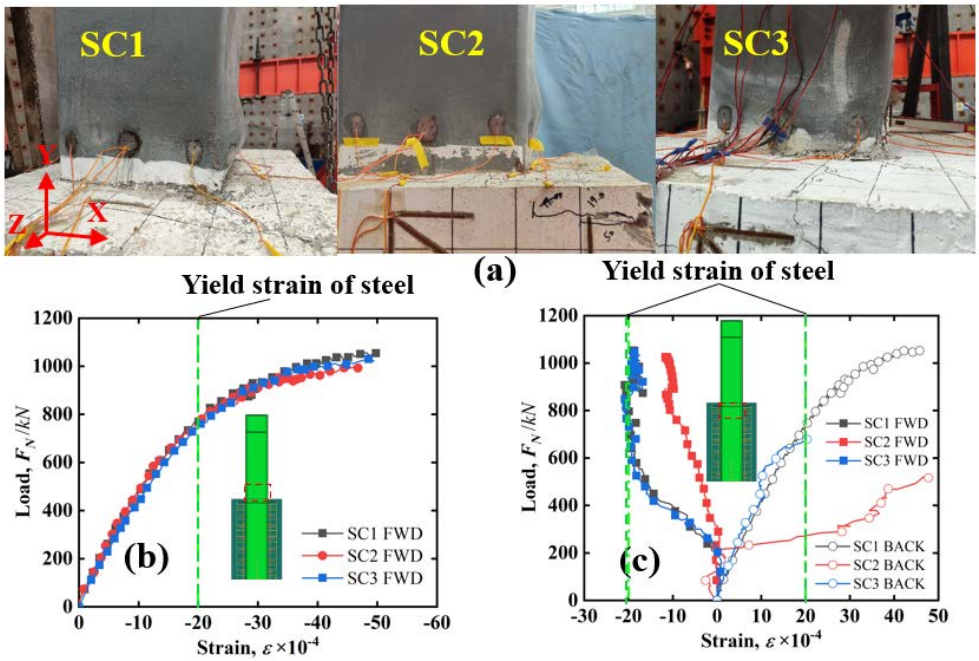

Figure 8. Buckling performance and strain comparison at the back side (BACK) and forward side (FWD) of specimens: (**a**) buckling performance, (**b**) upper steel tube, (**c**) lower steel tube.

3.2. Load~Displacement Curve

The load-top displacement curves of the specimens from tests were plotted in Figure 9. The load-displacement curve [27,28] typically includes the elastic stage, yielding stage, strain hardening stage, ultimate load stage, and failure stage, which can clearly reflect the state of the structure under stress. The load-displacement curves for SC1 and SC3 exhibit similar developmental trends. During the loading phase of SC1, an increase in stiffness was observed in the middle portion of the specimen due to the tightening of bolts. However, upon entering the strengthening stage, the load-displacement curve of SC1 closely overlapped with that of SC3. Both curves exhibited nearly identical initial stiffness, with SC3 displaying a smoother and more gradual load-displacement relationship, indicating that SC3's load transfer and force performance were more stable. The SC2 specimen, on the other hand, experienced a prolonged yielding stage with a lower load-bearing capacity, resulting in significant deformations during this phase. The peak load was observed when the top displacement approached 90 mm, at which point severe damage had occurred at the bottom of the specimen, as shown in Figure 6.

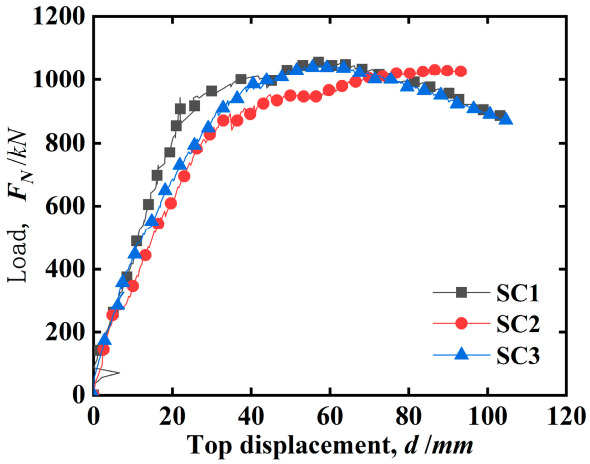

Figure 9. Load–displacement curves.

3.3. Loading Mechanism

As shown in Figure 10, the failure process of the three specimens can be categorized into four distinct stages: the elastic stage, yielding stage, strengthening stage, and failure stage. Using SC3 as an example, the load-strain curves of the most critical strain points in each part of the specimen were analyzed to investigate its loading mechanism. The magnitude of strain and the rate of strain increase (i.e., the slope of the curve) were employed to define the hierarchical relationships and magnitude of load transfer in each structural component, as illustrated in Figure 8.

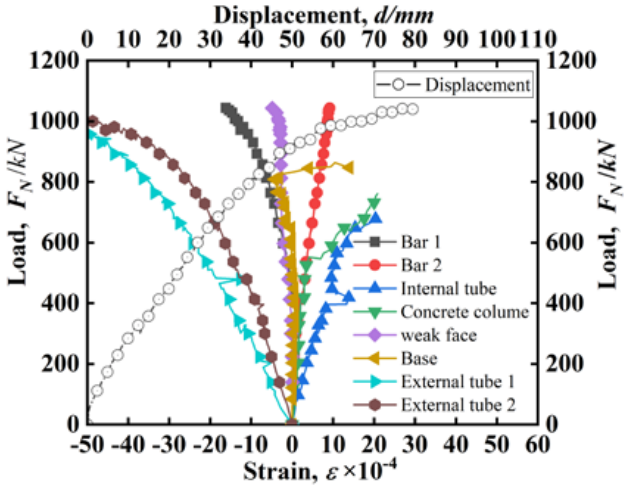

Figure 10. Loading mechanism analysis.

3.3.1. Elastic Stage (Load $\leq$ 600 kN)

During this phase, the specimen remained in the elastic range. The load was primarily carried by the lower part of the upper steel tube, with the back and front sides of the lower steel tube bearing portions of the forces generated by the steel tube's deformation. This resulted in significant tensile forces on the back side of the concrete column. The strain value at certain measurement points is 0.02%, which has reached the ultimate tensile strain of concrete. As the load exceeded 400 kN, forces in these areas increased further, and the slope of the load-strain curve for the lower backside of the concrete column increased significantly, at 600 kN, the maximum strain reached 0.09%.

3.3.2. Yielding Stage (600 kN $\leq$ Load $\leq$ 800 kN)

In this stage, a large number of cracks began to develop on the backside of the concrete column and quickly reached the ultimate tensile strain, leading to failure of the concrete in this region. The strain slope on the front side of the lower steel tube increased, and the strain rapidly increased from 0.13% to 0.2%, reflecting growing deformation. Strain in the lower back side of the lower steel tube increased rapidly until strain gauges were damaged, as indicated by the interruption of strain data in Figure 7. Strain in the concrete base also increased noticeably, accompanied by crack formation. The strain rate in the upper reinforcement of the column remained largely unchanged, indicating the effectiveness of the base stiffener plate in reinforcing the column base.

3.3.3. Strengthening Stage (Load > 800 kN)

As the load exceeded 800 kN, the specimen transitioned into the strengthening stage. The local strain in the lower part of the upper steel tube reached about 0.25% and increased rapidly until the bottom fully entered a yielding state. Concurrently, the concrete base exhibited an inflection point in its strain curve and failure. The strain in the upper reinforcement of the column increased significantly (-0.16%), although it did not yet reach the yield strain. Yielding deformation became pronounced in the lower part of the upper steel tube, leading to the ultimate failure of the specimen.

3.4. Effect of Filled Concrete and Encasement Thickness

Based on the analysis in the preceding sections and the materials selected for the working conditions in the test, it can be concluded that grouting does not effectively prevent the yielding of profile steel. Furthermore, the increased local stiffness within the specimen results in uneven load transfer, leading to damage in other parts of the structure. In practical construction, grouting introduces additional complexity and increases construction time. Alternatively, increasing the cross-sectional area of the concrete short column has been shown to effectively reduce the deformation of the square hollow steel-reinforced concrete column. Therefore, in engineering applications, it is critical to avoid uneven structural strength that may result in localized failure.

4. Numerical Investigation

4.1. Model Establishment

A numerical model of the square hollow steel-reinforced concrete column was first established based on experimental results. The 'Solid' element was employed to model the steel tube and the concrete, and the 'Truss' element was used to represent the reinforced bars. The steel tube and reinforced bars were modeled by an ideal elastic-plastic constitutive model, and the yield strength of the steel plate is 345 MPa, the elastic modulus is 2.06×10^5 MPa, and the Poisson's ratio is 0.3. The concrete behavior was simulated using the Concrete Damaged Plasticity (CDP) model proposed by Lubliner [29] and Lee [30], with different damage factors for tensile and compression damage [31]. It is assumed that cracks close and stiffness recovers when concrete is stretched into compression, while cracks persist from compression to tension, and stiffness does not recover. The CDP model ensures better convergence for both tensile and compressive behaviors of the concrete. The E modulus of concrete is taken as follows [32]:

$$E = \frac{10^5}{2.2 + 34.7/f_{cu}} \quad (1)$$

where f_{cu} the compressive strength of the concrete cube is, the Poisson ratio is 0.2, and plastic parameters are shown in Table 2.

Table 2. Plastic parameters of concrete.

Expansion Angle	Eccentricity	f_{b0}/f_{c0}	K	Adhesive Parameters
38	0.1	1.16	0.667	0.0005

where 'Expansion Angle' is the angle that defines the shape of the yield surface in the plastic model; 'Eccentricity' is the parameter that governs the shape of the yield surface in stress space; 'f_{b0}/f_{c0}' is the ratio of the initial tensile strength (f_{b0}) to the initial compressive strength (f_{c0}) of concrete; 'K' is the plastic hardening coefficient; 'Adhesive Parameters' is the bond strength between the concrete and reinforcement.

To address potential contact issues between materials and ensure model convergence, all contacting surfaces between steel materials were modeled as 'Tie' without accounting for welding residual stresses. The contacts of reinforced bars, cylinder studs and concrete were 'Embedded' within the concrete without considering slippage. The contacts between the concrete filled inside the square hollow steel tube was modeled as 'face-to-face', where the "Tangential Behavior" is set to "Penalty" with a friction coefficient of 0.5; the "Normal Behavior" is "Hard" Contact.

To address potential contact issues between materials and ensure model convergence, all connection surfaces between the profile steel were modeled using "Tie" connections, without accounting for welding residual stresses. Similarly, the interfaces between the profile steel and concrete were also modeled using "Tie" connections. The steel mesh, cylinder head weld studs, and support angle irons were "Embedded" within the concrete without considering slippage. The concrete filled inside the square hollow steel, and the inner surface of the square hollow steel was modeled as "face-to-face" contact.

To simplify the boundary condition and minimize the number of contact elements, the mechanical connections between the basement and the laboratory ground were omitted, and alternatively the deformation of the concrete base was modeled as fully fixed, except for the top surface. The horizontal force was applied through displacement loading in the X direction, with a total displacement of 120 mm. To simulate the effect of the constraint beam, a fixed boundary condition was applied at the top of the front side of the concrete column, as shown in Figure 11. To ensure a balance between computational efficiency and accuracy, the mesh was set to be 50 mm by 'Size' for simplicity. The same modeling approach was used to simulate the loading process of all specimens. In addition, the final results showed the reasonableness of this size in simulation.

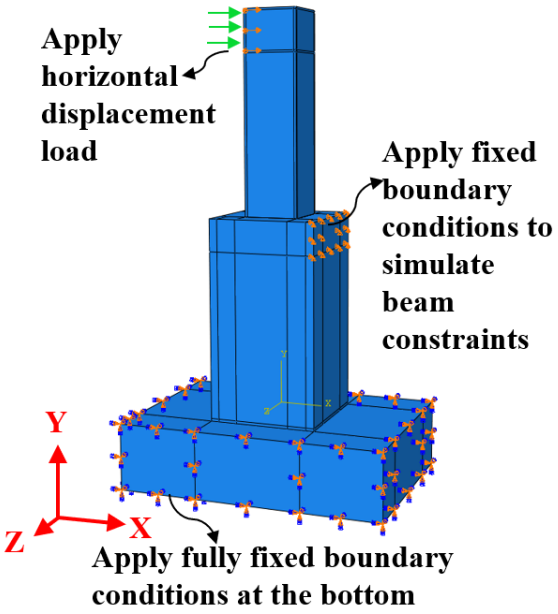

Figure 11. Numerical model used in this study.

4.2. Model Verification

The load-displacement curve of the specimen top was extracted and compared with the experimentally measured values in Figure 12. Additionally, the corresponding displacement contour map and the stress concentration area of the specimen during loading are also presented in the figure. Generally, the comparison indicates that the trends and the exact value of the load-displacement curve in simulation closely match those observed in the experimental results. The stress concentration area of the steel tube in the numerical model is essentially consistent with the final failure shape observed in the experiment. The initial stiffness obtained from the numerical analysis is slightly larger than that of the experimental results.

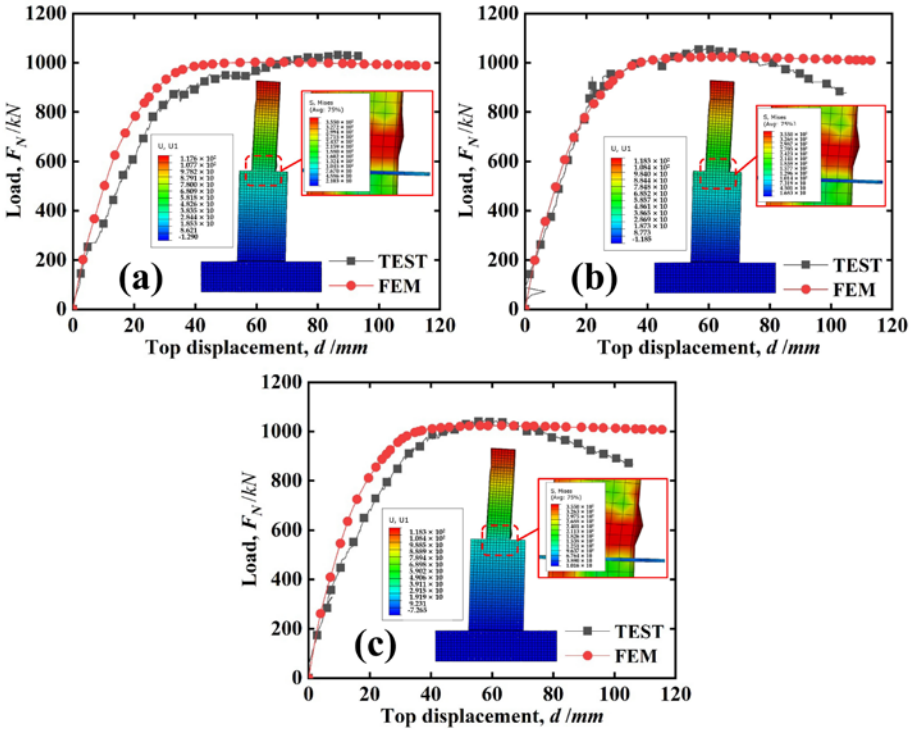

Figure 12. Comparison of bearing capacity curves between test and numerical model: (**a**) SC1, (**b**) SC2, (**c**) SC3.

There are possibly two reasons for this issue. First, when using 'Embedded', the slippage between concrete and steel bars/studs might be marginally underestimated in relation to the real case by numerical calculation. Second, the specimens may experience some inevitable damage during casting, transportation, and installation. Thus the true strength of the specimen would be smaller than the input value, resulting in a larger initial stiffness in numerical analysis. During the yielding and failure phase, the numerical model did not exhibit a noticeable drop of the load-displacement curve. This is primarily because the steel material was modeled by an ideal elastic-plastic constitutive model, with which the stress remains constant with strain after yielding stress. Overall, the numerical model adequately simulates the testing process of the specimens.

4.3. Parametric Study

4.3.1. Major Factors

With the verified model, a parametric study was performed in this section. The SC3 specimen was selected as the baseline model. Without significant change of SC3, three parameters: (1) concrete strength × 6, (2) steel tube strength × 6, and (3) thickness × 6 were varied in this section, and a total of 18 cases were designed. The parametric analysis

was performed using the peak load~displacement (F_M~d_M) as the indicator, and the output data of all the cases is presented in Table 3. The relationship of peak loading and peak displacement as per varied parameters is shown in Figure 13. From Figure 13a,d, it can be observed that both peak load and peak displacement kept almost constant with concrete strength: thus, concrete strength is not the primary factor affecting the critical state of square hollow steel-reinforced concrete columns. In practical situations, HSrCC is equipped with a stiff ground beam at the interface plate, where the concrete short columns can easily withstand the transmitted compressive forces. In comparison, the steel tube has a relatively weaker cross-sectional strength: therefore, the flexural capacity of HSrCC primarily relies on the strength of the steel.

Table 3. Design parameter values and main results.

No.	Concrete Strength, σ_c/Mpa	Tube Thickness, d_s/mm	Tube Strength, σ_s/Mpa	Peak Displacement, d_M/mm	Peak Load, F_M/kN
1	35	14	355	62.1	1023.5
2	40			61.9	1023.4
3	45			61.7	1023.2
4	50			61.5	1023.1
5	55			60.4	1023.2
6	60			61.1	1022.9
7	40	10	355	48.1	786.1
8		12		51.6	898.2
9		14		65.6	1103.6
10		16		93.8	1130.5
11		18		109.5	1230.1
12		20		142.4	1311.1
13	40	14	345	59.7	999.7
14			355	61.9	1023.4
15			390	65.6	1103.6
16			420	70.7	1169.7
17			460	90.4	1277.6
18			500	96.4	1358.8

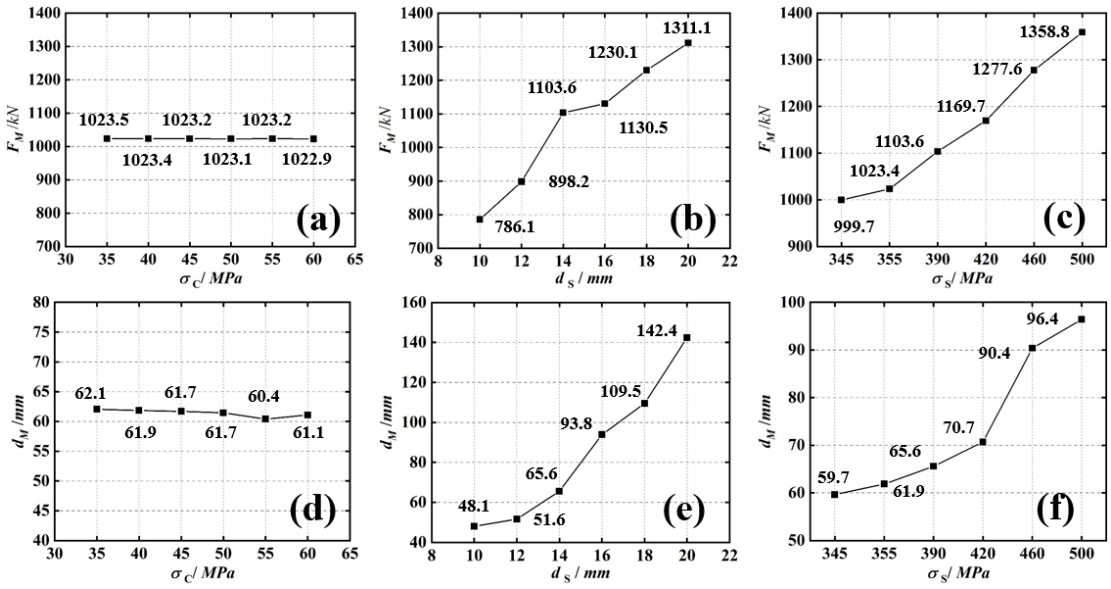

Figure 13. Peak loading as per (**a**) concrete strength, (**b**) tube thickness, (**c**) tube strength, and peak displacement as per (**d**) concrete strength, (**e**) tube thickness, (**f**) tube strength.

The relationship of peak loading and peak displacement as per varied tube thickness are shown in Figure 13b,e. Clearly, the tube thickness has a significant impact on peak loading and peak displacement. It can be concluded basically that increasing the tube thickness is able to enhance the performance of HSrCC. In addition, from the analysis of the curve's slope, it was found that the critical thickness of the specimen studied in this research is ranging from 14 to 16 mm. If carefully checking, when the thickness exceeds 14 mm, the peak displacement of the specimen increases noticeably, but the increment in peak load gradually slows down. The relationship of peak loading and peak displacement as per varied tube yield strength (e.g., from Q345 to Q500) are shown in Figure 13c,f. As the strength increases, peak load gradually increases with a constant slope. However, the displacement turns to rapid increment from 70 mm to 90 mm with Q420 to Q460. This result indicates that for the square HSrCC used in this research, a tube with Q355 to Q420 was recommended without significant displacement.

4.3.2. Peak Load Estimation

As the concrete strength is not a sensitive factor to the peak load of the half-encased square HSrCC in this study, thus by taking the tube thickness and strength as variables, linear regression analysis of the peak load was performed in this section using the least squares method (LSM) [33]. The Formula (2) is the relationship between y and x (x_1, x_2, x_3). Formula (3) is the matrix representation of Formula (2). The solution for β (Formula (4)) can be calculated using LSM.

$$y = \beta_0 + \beta_1 x_1 + \beta_2 x_2 + \varepsilon \tag{2}$$

$$Y = X\beta + \varepsilon \tag{3}$$

$$\hat{\beta} = \left(X^T X\right)^{-1} X^T Y \tag{4}$$

where y is the dependent variable, and x_1, x_2, x_3, ... are the independent variables; Y is the vector of the dependent (response) variable; X is the design matrix containing the data for all independent (predictor) variables; β is the vector of regression coefficients; ϵ is the vector of error terms.

The final equation can be obtained as follows:

$$F_M = -536 + 52.18\, d_s + 2.335\, \sigma_s \tag{5}$$

The analytical results of peak value for the cases in Section 4.3.1 were compared with the simulation results, as shown in Figure 14. In general, the analytical values are close to the simulation values.

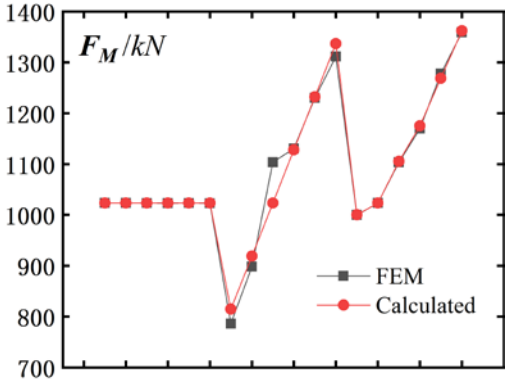

Figure 14. Comparison of calculated and simulated values.

4.3.3. Verification

To verify the applicability of the formula, random values of tube thickness and strength were selected (Table 4), and simulations were performed using the same model as Figure 11. The calculated and analytical results of peak value are shown in Table 4. The comparison between the numerical results and the calculated results is shown in Figure 15. From Figure 15, it was known that the two curves in general match with each other. The maximum error is 5.06% among the randomly designed cases. We can conclude that the formula is applicable for calculating the bearing capacity of this structure.

Table 4. The calculation results of random parameters.

Number	Thickness/mm	Strength/MPa	Calculated/kN	Simulation/kN	Error
FEM-1	14	420	1175.2	1169.7	0.47%
FEM-2	18	345	1208.8	1203.1	0.47%
FEM-3	12	500	1257.7	1194.1	5.06%
FEM-4	16	460	1373.0	1372.0	0.07%
FEM-5	12	460	1164.3	1123.3	3.52%

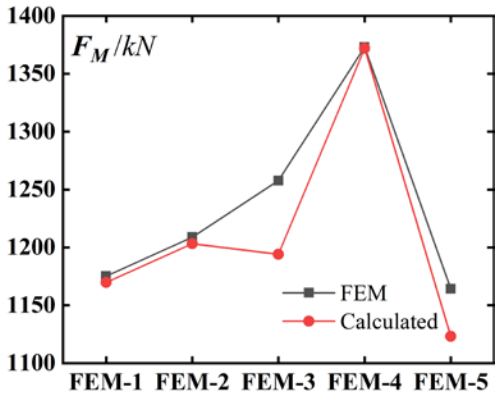

Figure 15. Comparison of peak load of random cases by proposed equation and simulation.

4.4. Discussion: Implication, Limitation, and Prospects

The empirical formula obtained from this study can be applied during the design phase. With known tube thickness and yield strength, the maximum loading that could be applied can be estimated by Formula 5. In addition, similar equations can be obtained for different dimensions of HSrCC specimens to direct the design further. All in all, the research methodology is applicable to similar structures.

Of note, the fitted formula in this paper is applicable only for calculating the load-bearing capacity of HSrCC under the dimensions in this study. However, a larger or smaller encasement thickness, or varied tube sections, may yield a different result.

In this paper, only the lateral resistance of the HSrCC was studied. A more comprehensive investigation related to the performance of HSrCC under combined loading, e.g., lateral and axial loading or lateral loading and bending, should be conducted in the further

5. Conclusions

This study investigates the stress performance of square hollow steel-reinforced concrete columns (HSrCC) with fragile cross-sections under bending and shear forces using testing and finite element methods. Based on the results, the main conclusions are summarized as follows:

(1) Form the experimental results, it was found, the crack propagation of the specimen can be divided into five steps: initial crack between encased concrete and tube; transverse

crack at top of concrete column; transverse crack on the side surface of concrete column; crack of concrete base; crushing at con-strained beam.

(2) Comparison indicated that filling concrete or not will not significantly impact the strength and failure of HSrCC. In addition, increasing the cross-sectional area of the concrete short column can effectively reduce the deformation of the square HSrCC.

(3) Numerical study found that the resistance strength of HSrCC was dominated by the tube rather than the encased concrete. This is related to the structural design in practice. Larger tube thickness and steel yield strength resulted in a higher resistance. The optimal steel tube thickness is 14~16 mm with tube strength ranging from Q355 to Q420 considering the HSrCC in this study.

(4) The peak load calculation formula derived in this study demonstrates high accuracy, with a calculation error of less than 5.06% compared to numerical analysis results within the tested parameter range.

Author Contributions: Conceptualization, H.L. and Y.Z.; methodology, Y.Z.; software, S.G.; validation, S.G.; formal analysis, H.Q.; investigation, S.G. and H.Q.; resources, H.L.; data curation, J.L. and X.W.; writing—original draft preparation, H.L. and Y.Z.; writing—review and editing, Y.Z. and J.L.; visualization, X.W.; supervision, H.L.; project administration, Y.Z.; funding acquisition, H.L. All authors have read and agreed to the published version of the manuscript.

Funding: This research was funded by [Backbone Training Program of Young Researchers in Henan University of Technology] grant number [21420194], [Henan Province Science and Technology R&D Program Joint Fund] grant number [232103810078], [Henan Key Laboratory of Grain and Oil Storage Facility and Safety] grant number [2022KF04], and [Zhengzhou R&D Special Grants for Scientific Research] grant number [22ZZRDZX38].

Data Availability Statement: The data used to support the findings of this study are available from the corresponding author upon request.

Acknowledgments: We gratefully acknowledge the Henan Key Laboratory of Grain and Oil Storage Facility and Safety. Special thanks to Hongkai Wang for his assistance with this research.

Conflicts of Interest: Author Hulin Li, Haijiang Qin, Xiong Wang and Jinpeng Li was employed by the company Shanghai Baoye Group Corp., Ltd. The remaining authors declare that the research was conducted in the absence of any commercial or financial relationships that could be construed as a potential conflict of interest.

References

1. Xiamuxi, A.; Wang, Z.; Yang, B. Optimum reinforcement ratio of axially loaded reinforced concrete-filled square steel tube column. *J. Constr. Steel Res.* **2023**, *203*, 107805. [CrossRef]
2. Yang, Z.; Liu, M.; Sun, L.; Shen, M. Size effect of axial compressive bearing capacity of high-strength concrete filled high-strength square steel tubular short columns. *Structures* **2024**, *60*, 105978. [CrossRef]
3. Ding, F.-x; Fang, C.; Bai, Y.; Gong, Y.-z. Mechanical performance of stirrup-confined concrete-filled steel tubular stub columns under axial loading. *J. Constr. Steel Res.* **2014**, *98*, 146–157. [CrossRef]
4. He, F.; Li, C.; Chen, B.; Liu, J.; Zhang, M.; Briseghella, B. Compressive behavior of concrete-encased CFST column with initial stress. *J. Constr. Steel Res.* **2023**, *201*, 107724. [CrossRef]
5. Wei, Y.; Jiang, C.; Wu, Y.-F. Confinement effectiveness of circular concrete-filled steel tubular columns under axial compression. *J. Constr. Steel Res.* **2019**, *158*, 15–27. [CrossRef]
6. Chen, H.; Liao, F.; Yang, Y.; Ren, Y. Behavior of ultra-high-performance concrete (UHPC) encased concrete-filled steel tubular (CFST) stub columns under axial compression. *J. Constr. Steel Res.* **2023**, *202*, 107795. [CrossRef]
7. Shen, Q.; Li, K.; Wang, J.; Wang, F.; Hu, Z.; Li, G. Cyclic behaviour of circular CFT-SG columns under axial tension-compression: Novel FE modelling and design methods. *Structures* **2024**, *62*, 106148. [CrossRef]
8. Mata, R.; Nuñez, E. Cyclic Behavior of Concrete-Filled Tube Columns with Bidirectional Moment Connections Considering the Local Slenderness Effect. *Buildings* **2024**, *14*, 2240. [CrossRef]

9. Shen, Q.; Li, K.; Zhu, W.; Wang, J.; Li, J. Lateral impact behaviour of CCFT columns with spherical-cap gap imperfection: Numerical modelling and design method. *Structures* **2023**, *58*, 105455. [CrossRef]
10. Al-Rousan, R.; Nusier, O.; Abdalla, K.; Alhassan, M.; Lagaros, N.D. NLFEA of Sulfate-Damaged Circular CFT Steel Columns Confined with CFRP Composites and Subjected to Axial and Cyclic Lateral Loads. *Buildings* **2022**, *12*, 296. [CrossRef]
11. Lee, H.-J.; Choi, I.-R.; Oh, M.-W. Vertical diaphragms for moment connection of thin-walled CFT column to steel beam. *J. Build. Eng.* **2024**, *97*, 110607. [CrossRef]
12. Tong, L.; Zheng, J.; Wu, H.; Wang, K.; Dong, B.; Liu, B. Parametric study of steel-beam to flat-rectangular CFST column connections with small-size diaphragms. *J. Constr. Steel Res.* **2023**, *211*, 108156. [CrossRef]
13. Nguyen-The, D.; Thai, S.; Nguyen-Van, H.; Ngo-Huu, C. Numerical Modelling of the Punching Shear Response of Shearhead Connections between a CFT Column and a Flat Reinforced Concrete Slab. *Struct. Eng. Int.* **2024**, 1–15. [CrossRef]
14. Lee, H.J.; Park, H.G.; Choi, I.R.; Hwang, H.J. Tensile and flexural behaviors of connections between steel beam and concrete-encased-and-filled steel tube column. *J. Build. Eng.* **2022**, *49*, 104042. [CrossRef]
15. Duan, Y.; Cheng, M.; Hu, Y.; Zhang, Y. Seismic behavior analysis of concrete-filled square steel tubular column-steel beam connections. *Shanxi Archit.* **2018**, *44*, 44–45. (In Chinese)
16. Han, L.; Liu, W.; Yang, Y. Behaviour of concrete-filled steel tubular stub columns subjected to axially local compression. *J. Constr. Steel Res.* **2008**, *64*, 377–387. [CrossRef]
17. Yang, Y.-F.; Han, L.-H. Behaviour of concrete filled steel tubular (CFST) stub columns under eccentric partial compression. *Thin-Walled Struct.* **2011**, *49*, 379–395. [CrossRef]
18. Wang, Y.; Yang, Y.; Zhang, S. Static behaviors of reinforcement-stiffened square concrete-filled steel tubular columns. *Thin-Walled Struct.* **2012**, *58*, 18–31. [CrossRef]
19. Abbas, H.; Siddiqui, N.A.; Khateeb, B.M.; Almusallam, T.H.; Al-Salloum, Y.A. Performance of new CFST square column-to-foundation connections for cyclic loads. *J. Constr. Steel Res.* **2021**, *185*, 106868. [CrossRef]
20. Zhang, W.; Gardner, L.; Wadee, M.; Chen, K.; Zhao, W. On the uniform torsional rigidity of square concrete-filled steel tubular (CFST) sections. *Structures* **2022**, *43*, 249–256. [CrossRef]
21. Jia, Z.-L.; Wang, W.-D.; Shi, Y.-L.; Xian, W. Performance of steel-reinforced concrete-filled square steel tubular members under sustained axial compression loading. *Eng. Struct.* **2022**, *264*, 114464. [CrossRef]
22. Zhou, Z.; Zhou, X.; Yan, B.; Gan, D. Shear strength of stiffened square thin-walled concrete-filled steel tubular columns. *J. Build. Eng.* **2022**, *58*, 104968. [CrossRef]
23. Hu, C.; Wang, Y.; Cheng, R.; Luo, J.; Gong, M. Confinement effect and stress-strain model for concrete of multi-cell CFST column under axial compression. *J. Constr. Steel Res.* **2024**, *221*, 108865. [CrossRef]
24. Kopraman, Y.; Özdemir, A.; Anıl, Ö.; Sakin, S.; Armakan, F. Experimental investigation of bond–slip behavior of between-anchored steel strips to concrete surface. *Arch. Civ. Mech. Eng.* **2022**, *22*, 198. [CrossRef]
25. Ghoroubi, R.; Mercimek, Ö.; Özdemir, A.; Anil, Ö. Experimental investigation of damaged square short RC columns with low slenderness retrofitted by CFRP strips under axial load. *Structures* **2020**, *28*, 170–180. [CrossRef]
26. Zhang, H.; Wang, H.; Zhou, Y.; Chang, Z. Waterproofing performance of polypropylene—Concrete wall of underground silo under combined compressive stress and water pressure. *Heliyon* **2022**, *8*, e12074. [CrossRef]
27. Kolesnikov, G. Analysis of Concrete Failure on the Descending Branch of the Load-Displacement Curve. *Crystals* **2020**, *10*, 921. [CrossRef]
28. Zhang, H.; Wang, H.; Yang, J.; Wang, F. A novel vertical waterproofing joint with trapezoidal steel plate connections for steel–concrete underground silos: Bending test and numerical simulation. *Tunn. Undergr. Space Technol.* **2023**, *137*, 105150. [CrossRef]
29. Lubliner, J.; Oliver, J.; Oller, S.; Oñate, E. A plastic-damage model for concrete. *Int. J. Solids Struct.* **1989**, *253*, 299–326. [CrossRef]
30. Lee, J.; Fenves, G.L. Plastic-damage model for cyclic loading of concrete structures. *J. Eng. Mech.* **1998**, *124*, 892–900. [CrossRef]
31. Sidoroff, F. Description of Anisotropic Damage Application to Elasticity. In *Physical Nonlinearities in Structural Analysis*; Springer: Berlin/Heidelberg, Germany, 1981; pp. 237–244.
32. SIMULIA. *ABAQUS 6.14 Scripting User's Manual*; SIMULIA: Maastricht, The Netherlands, 2014.
33. Draper, N.R.; Smith, H. *Applied Regression Analysis*; Wiley Series in Probability and Statistics; McGraw-Hill Inc.: New York, NY, USA, 1998.

Disclaimer/Publisher's Note: The statements, opinions and data contained in all publications are solely those of the individual author(s) and contributor(s) and not of MDPI and/or the editor(s). MDPI and/or the editor(s) disclaim responsibility for any injury to people or property resulting from any ideas, methods, instructions or products referred to in the content.